Microchimica Acta (2026) 193:324
https://doi.org/10.1007/s00604-026-08007-5

RESEARCH

$(Cu–S)_n$ MOF–polyaniline based dual-platform biosensing for blood plasma and urine detection of ESAT-6 toward early tuberculosis diagnosis

Pei-Hsuan Chiang[1] · Zhi-Rou Liang[1] · Yi-Hua Lu[1] · Shi-Han Chen[1] · Ruei-Ting Tang[1] · Yuan-Hsiang Yu[1] · Mei-Lin Ho[1]

Received: 5 February 2026 / Accepted: 17 March 2026 / Published online: 20 April 2026

Abstract

Early and accessible diagnosis of tuberculosis (TB) remains a global health challenge, particularly in low- and middle-income countries. Early Secreted Antigenic Target 6 kDa (ESAT-6), released during initial infection, is a promising biomarker for TB detection. However, most current assays for TB detection depend on complex instrumentation and trained personnel, limiting their utility in resource-constrained settings. Here, we developed dual biosensing platforms based on a $(Cu–S)_n$ metal-organic framework–polyaniline (MOF–PANI) composite for ESAT-6 detection in blood plasma and urine. A paper-based microfluidic resistive immunosensor with pulsed light sintering optimization enabled quantification through resistance changes, achieving a detection range of 195 pM–50 nM with a limit of detection (LOD) of 39.2 pM in human blood plasma. In parallel, a glassy carbon electrode–based electrochemical sensor was fabricated by covalent antibody immobilization on MOF–PANI, followed by bovine serum albumin (BSA) blocking. Cyclic voltammetry revealed a detection range of 23.6 fM–1.56 nM with an ultralow LOD of 1.68 fM in artificial urine, along with excellent reproducibility and stability. Together, these results highlight the versatility of MOF–PANI composites in enabling multi-matrix ESAT-6 detection, offering complementary advantages of blood plasma-based point-of-care testing and urine-based non-invasive diagnostics. This integrated strategy shows strong potential for scalable, accessible, and accurate early TB diagnosis.

Keywords Tuberculosis diagnosis · $(Cu–S)_n$ MOF–polyaniline composite · Paper-based microfluidics · Electrochemical biosensor · Glassy carbon electrode–based sensor · Blood plasma and urine analysis · Pulsed light sintering optimization

Introduction

Tuberculosis (TB) remains one of the leading causes of infection-related mortality worldwide, second only to COVID-19 in 2020, with the greatest burden concentrated in low- and middle-income countries [1]. Early detection of TB is essential to ensure timely treatment, curb transmission, and improve patient outcomes [2]. In resource-limited settings, the need for affordable, user-friendly, and accessible diagnostic technologies has become increasingly critical [3]. Among the available biomarkers, Early Secreted Antigenic Target 6 kDa (ESAT-6) is secreted exclusively by virulent *Mycobacterium tuberculosis* (MTB), minimizing cross-reactivity and boosting assay sensitivity. As an early infection marker, ESAT-6 appears in host fluids even at low bacterial loads, making it highly suitable for early TB diagnosis [4]. However, most current detection methods rely on complex instrumentation and trained personnel, limiting their accessibility in resource-constrained setting [5]. These challenges highlight the urgent need for versatile and accessible biosensing strategies capable of detecting ESAT-6 across different biological fluids, thereby supporting both point-of-care and non-invasive diagnostic applications.

✉ Yuan-Hsiang Yu
084916@mail.fju.edu.tw

✉ Mei-Lin Ho
157382@mail.fju.edu.tw

[1] Department of Chemistry, Fu Jen Catholic University, New Taipei City 242, Taiwan

Point-of-care (POC) devices have gained prominence as effective tools for the rapid and accurate detection of TB, addressing critical healthcare challenges in resource-limited settings. Several POC testing (POCT) methods have been developed, including lateral flow assays for detecting lipoarabinomannan (LAM) antigen in urine and loop-mediated isothermal amplification (LAMP) for identifying MTB complex DNA in sputum [5]. Additional approaches, such as point-of-care ultrasound (POCUS), nucleic acid amplification tests (NAATs), and optical-based devices, have also been explored for TB screening [3]. Despite these advances, many POCT strategies still face limitations in sensitivity, specificity, and adaptability across diverse clinical contexts. Importantly, non-invasive specimens such as urine [6] and minimally invasive matrices like blood plasma offer clear advantages in terms of safety, accessibility, and patient compliance, yet remain underutilized in current diagnostic workflows. These gaps underscore the urgent need for innovative biosensing technologies that integrate versatility, high sensitivity, and practicality to advance early TB diagnosis.

Emerging technologies are revolutionizing TB diagnosis and management [7], with metal-organic frameworks (MOFs) recognized as promising materials due to their tunable structures and high surface areas [6], [8]. MOFs have been successfully integrated into diverse biosensing platforms, including paper-based devices for portable and low-cost diagnostics as well as electrochemical sensors for highly sensitive biomarker detection [9], [10] and [11]. Unlike conventional MOFs, which are typically electrical insulators, conductive metal-organic frameworks (CMOFs) exhibit enhanced electrical conductivity, making them particularly attractive for resistive electrochemical sensing applications [12]. A notable advancement involves the structural evolution of copper-based MOFs with two-dimensional $(–Cu–S–)_n$ networks, enabling multidirectional charge transfer and achieving an electrical conductivity of 10.96 S cm^{-1} in a single-crystal CMOF [13]. Building on these properties, a semiconductive $(Cu–S)_n$ MOF–polyaniline (PANI) nanocomposite for hydrogen sulfide (H_2S) gas sensing was reported, which showed a 3.4-fold higher sensitivity than PANI-coated interdigitated electrodes (IDEs) due to enhanced conductivity and optimized band gap hybridization [14]. These advancements highlight the potential of $(Cu–S)_n$ MOF–PANI composites to enable scalable and versatile TB diagnostics, particularly through dual-platform applications for detecting ESAT-6 in both blood plasma and urine samples.

To date, the integration of conductive $(Cu–S)_n$ MOFs with polymer composites for multi-matrix TB diagnostics remains unexplored. In this work, we report a novel dual-platform biosensing strategy based on $(Cu–S)_n$ MOF–PANI composites, where pulsed light sintering (PLS) was strategically employed to precisely modulate the material's conductivity and surface properties. This advanced processing technique significantly enhanced the analytical sensitivity, enabling the detection of the ESAT-6 biomarker across two distinct modalities. First, a paper-based microfluidic resistive immunosensor was developed for POCT in human blood plasma, reaching a pM-level LOD. Second, an electrochemical sensing platform using glassy carbon electrodes (GCE) was constructed, achieving an ultralow fM-level LOD for non-invasive ESAT-6 detection in urine. We further demonstrate how the PLS treatment and platform-specific surface modifications lead to unique selectivity profiles for each matrix. By benchmarking against enzyme-linked immunosorbent assay (ELISA) and validating with clinical-range concentrations, this dual-platform approach offers a versatile, scalable, and high-performance solution for early TB diagnosis in both resource-limited and clinical settings.

Experimental sections

Materials

Phosphate-buffered saline (PBS, 10 mM, pH 7), sourced from Biomate, was used for sample dilution and microenvironment stabilization in ESAT-6 detection experiments. 1-(3-Dimethylaminopropyl)−3-ethylcarbodiimide Hydrochloride (EDC) was purchased from TCI, and Nafion was purchased from DuPont de Nemours. Camphorsulfonic acid ((1 S)-(+)-CSA), N-hydroxysuccinimide (NHS), Glutaraldehyde, bovine serum albumin (BSA), ascorbic acid (AA), glucose (Glu), human serum albumin (HSA), Urea, Uric acid, Glycine (Gly), Methionine (Met), L-Aspartic acid (Asp), L-Tryptophan (Trp) were from Sigma-Aldrich. Alcohol was procured from J.T. Baker. Rabbit ESAT-6 Polyclonal Antibody (Ab), ESAT-6 recombinant protein, TB CFP10 Recombinant Protein (CFP-10), MPT-64 recombinant protein (MPT-64), ESAT6-CFP10 recombinant protein (ESAT-6-CFP-10 hybrid), and human ESAT-6 ELISA kit 96-well test were from MyBioSource. L-valine (Val) and Potassium hexacyanoferrate(II) trihydrate ($K_4[Fe(CN)_6]\cdot 3H_2O$) were from Alfa Aesar. Artificial urine was from Pickering Laboratories. Potassium hexacyanoferrate(III) ($K_3[Fe(CN)_6]$) was from Acros Organics.

Fabrication of the $(Cu–S)_n$ MOF–PANI paper-based biosensor

Polyaniline (PANI) and $(Cu–S)_n$ metal–organic framework ($(Cu–S)_n$ MOFs) were used as control materials, while a nanocomposite containing 5 wt% $(Cu–S)_n$ MOFs within PANI ($(Cu–S)_n$ MOF–PANI) served as the test group. The $(Cu–S)_n$ MOFs were synthesized as described in our previous report [14]. For sensor fabrication, a 16 wt%

camphorsulfonic acid (CSA) solution was prepared in ethanol. Subsequently, 6.5 wt% of $(Cu–S)_n$ MOF–PANI was added to CSA solution, stirred, and centrifuged at 700 rpm for 15 min; the supernatant was collected as the $(Cu–S)_n$ MOF–PANI solution. Control solutions of pure PANI and pure $(Cu–S)_n$ MOFs were prepared in the same way, except that MOFs were used directly without centrifugation.

The paper-based microfluidic device was fabricated using a wax printing method to create a convex pattern consisting of an injection zone (0.3 cm in diameter) and a detection zone (1.0 × 0.9 cm). The wax-printed paper was heated to promote wax penetration, ensuring hydrophobic channel boundaries. Onto the detection zone, 10 µL of the $(Cu–S)_n$ MOF–PANI solution was drop-cast and subjected to photonic sintering with a xenon pulse light system (PLS) to enhance electrical conductivity. The surface was then modified with 5 µL of EDC-NHS solution, followed by immobilization of 5 µL of ESAT-6 Ab. Nonspecific binding sites were blocked with 5 µL of BSA. In the injection zone, 1 µL of Nafion was applied as a filtration layer. In the paper-based biosensor, resistance changes were monitored, whereas in the electrochemical biosensor, oxidation peak currents were measured.

For electroresistance measurements, conductivity changes were recorded in the detection zone using a four-point probe method. The resistance as R_1 of the sintered $(Cu–S)_n$ MOF-PANI film was measured. After which 5 µL of ESAT-6 antigen at varying concentrations was introduced into the injection zone, the resulting resistance was recorded as R_2. The percentage change in resistance (ΔR) was calculated according to Eq. (1):

$$\Delta R = R_2 - R_1 \quad (1).$$

Fabrication of the $(Cu–S)_n$ MOF–PANI electrochemical biosensor

GCE were polished with 0.3 and 0.05 µm alumina slurries, rinsed with deionized water, and dried under nitrogen. A 5 µL aliquot of the $(Cu–S)_n$ MOF–PANI composite solution (prepared as in Fabrication of the $(Cu–S)_n$ MOF–PANI paper-based biosensor, but at a centrifugation speed of 6000 rpm) was drop-cast onto the GCE surface and dried at room temperature. The electrodes were activated with EDC and NHS in 10 mM PBS, followed by incubation with 7 µL of ESAT-6 Ab for 1 h. Non-specific binding sites were blocked with 5 µL of BSA for 1 h, and the electrodes were rinsed with PBS. Control electrodes with pure PANI or $(Cu–S)_n$ MOFs were prepared similarly. Cyclic voltammetry (CV) was used to characterize the electrodes and monitor ESAT-6 binding responses.

For material optimization, the oxidation peak current change ($\Delta I = I_1 - I_2$) was evaluated using CV, where I_1 was the peak current of the unmodified 5 wt% $(Cu–S)_n$ MOF–PANI/GCE, and I_2 was the peak current under varied conditions (e.g., different EDC-NHS volumes). For the calibration curve the current change was defined as $\Delta I = I_2 - I_1$, and recovery tests the current change was defined as $\Delta I = I_1 - I_2$, where I_2 was the peak current of ESAT-6/BSA/Ab/EDC-NHS/$(Cu–S)_n$ MOF–PANI/GCE, and I_1 was that of PBS/BSA/Ab/EDC-NHS/$(Cu–S)_n$ MOF–PANI/GCE. This enabled the assessment of the sensor's response to ESAT-6 at varying concentrations.

Instruments

A solid-ink printer (Fuji Xerox ColorQube 8570) was used to fabricate paper-based microfluidic channel patterns. A high-speed compact centrifuge (HITACHI CF15RXII) was used to prepare the 5 wt% $(Cu–S)_n$ MOF–PANI suspension. A xenon pulse light sintering system (Xenon X-1100) was employed to rapidly sinter 5 wt% $(Cu–S)_n$ MOF–PANI material on the test paper. A four-point probe measurement system (Keithley Model 2000) was utilized to measure the electrical resistance of the paper. Electrochemical measurements, including CV, was conducted using a potentiostat (PGSTAT204, Metrohm, Switzerland) controlled by Nova 2.0 software. A three-electrode system was employed, comprising a Ag/AgCl reference electrode, a GCE as the working electrode, and a platinum (Pt) counter electrode. Surface morphology and elemental composition of the paper-based biosensor were characterized using a field-emission scanning electron microscope (FE-SEM, JEOL JSM7600F and HITACHI S-3000 N) and X-ray photoelectron spectroscopy (XPS) with a high-throughput lab-based HAXPES spectrometer (ULVAC-PHI Quantes). Attenuated Total Reflection Fourier Transform Infrared Spectroscopy (ATR-FTIR, ABB FTLA2000-104) was applied to identify the functional groups on the sensor surface. Ultraviolet visible (UV–VIS) reflection was measured with a Hitachi U-4100.

Real samples analysis

To evaluate the analytical robustness and clinical applicability of the dual-platform biosensors, the recovery of ESAT-6 was investigated in human blood plasma and artificial urine. To accurately simulate clinical conditions and assess matrix effects, the analytical workflow commenced with spiking the target antigen into undiluted biological matrices before any subsequent processing or molecular recognition steps. The spiking concentrations were selected to encompass the clinically relevant ranges for tuberculosis-associated ESAT-6, facilitating early non-sputum-based TB diagnosis.

Paper-based biosensor

To assess the performance in a blood-based matrix, undiluted human blood plasma samples were first spiked with ESAT-6 at target concentrations. Following this initial

spiking step, the samples were diluted 25-fold with PBS (pH 7.0) to achieve a final sample-to-total volume ratio of 1:25 (v/v), with final ESAT-6 concentrations ranging from 0.78 to 50 nM (26.2 to 1690 ng/mL).

For validation, the results from the proposed resistive sensor were benchmarked against a commercial ELISA kit (Cat. No. MBS2607284, MyBioSource). Since the dynamic range of the ELISA kit is 1.56–100 ng/mL, samples exceeding this range were appropriately diluted with sample diluent. The final concentrations determined by ELISA were back-calculated using the respective dilution factors to verify the accuracy and methodological recovery of our paper-based platform.

Electrochemically based biosensor

The applicability for non-invasive diagnostics was evaluated using artificial urine. The raw artificial urine was spiked with ESAT-6 standard solutions at the beginning of the workflow. These spiked matrices were then subjected to a 40-fold total dilution. The final concentrations of ESAT-6 in the test samples ranged from 23.6 fM to 1.56 nM (0.799 pg/mL to 52.84 ng/mL). Prior to detection, the spiked samples were mixed with an equal volume of 20 mM $[Fe(CN)_6]^{3-/4-}$ solution as the redox probe for CV measurements. This procedure ensured that the sensor's sensitivity and selectivity were evaluated under conditions accounting for the complex ionic environment of urine.

To further evaluate the reproducibility and stability of the developed sensor, all spike-recovery experiments were performed in triplicate. The analytical performance was assessed by calculating the recovery and relative standard deviation (RSD) of the measured ESAT-6 concentrations.

Results and discussion

Fabrication of the paper-based biosensor

Scheme 1 illustrates the architecture of the paper-based microfluidic biosensor, comprising an injection zone, a detection zone, and wax-printed microchannels for directional flow. A thin Nafion layer was coated along the channels to suppress blood plasma-derived interferents, thereby improving selectivity [15], [16]. In the detection zone, the $(Cu–S)_n$ MOF–PANI nanocomposite was deposited and photonic-sintered, forming a continuous conductive network with low sheet resistance (≈30 Ω/sq). This enabled reliable resistance-based readouts, with distinct resistance shifts observed upon exposure to ESAT-6, confirming the feasibility of the device for blood plasma testing.

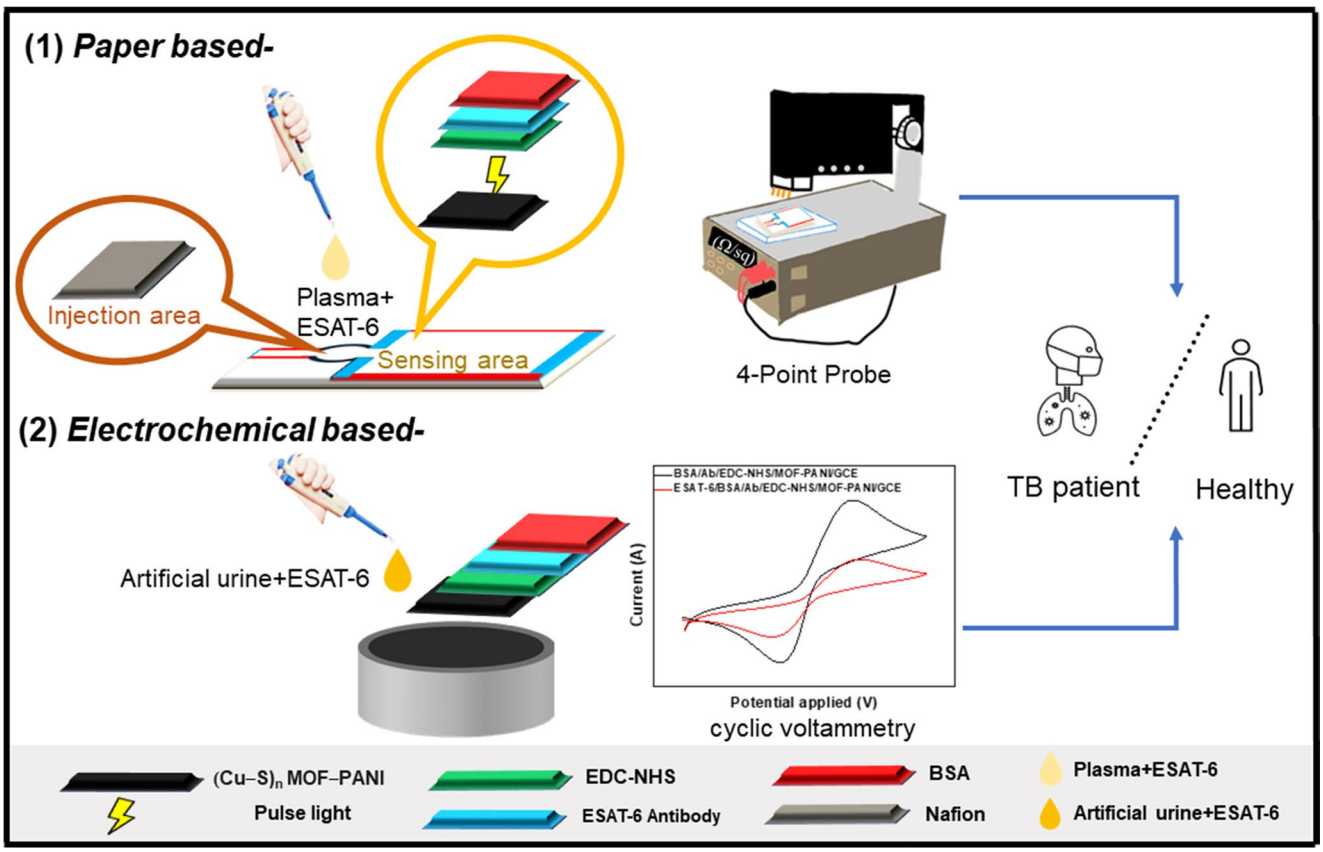

Scheme 1 Schematic illustration of the $(Cu–S)_n$ MOF–PANI (1) paper- and (2) electrochemical-based biosensor fabrication and detection workflow

Fabrication of the electrochemical biosensor

For the electrochemical platform (Scheme 1), the $(Cu–S)_n$ MOF–PANI composite was drop-cast onto a GCE to form a thin conductive sensing layer. In contrast to the paper-based system, this platform required neither photonic sintering nor Nafion treatment. Control electrodes composed of pure PANI or $(Cu–S)_n$ MOFs were prepared using the same procedure. CV was employed to characterize the electrochemical properties of the modified electrodes and to evaluate their responses to ESAT-6 binding. Although the incorporation of a Nafion film on the electrode surface was evaluated, the resulting film masked active reaction sites and impeded electron transfer, thereby suppressing the sensing signal and rendering the platform unsuitable for ESAT-6 detection. Electrodes were functionalized by sequential EDC-NHS activation, covalent immobilization of ESAT-6 antibodies, and BSA blocking to minimize nonspecific adsorption. CV measurements revealed that incorporation of MOFs into PANI enhanced conductivity and charge transfer, producing stronger and more reproducible oxidation peak currents compared with electrodes fabricated from PANI or MOFs alone.

Comparative evaluation and design optimization

To identify the optimal sensing matrix, three materials—$(Cu–S)_n$ MOFs, PANI, and their composite ($(Cu–S)_n$ MOF–PANI)—were systematically evaluated on both platforms. PANI was pre-functionalized with glutaraldehyde to enable antibody attachment.

Paper-based biosensor

To further isolate the impact of PLS, we evaluated the $(Cu–S)_n$ MOF–PANI composite performance with and without photonic sintering. Control experiments revealed that without PLS treatment, the composite suffered from macroscopic cracking and delamination upon drying, leading to poor substrate adhesion. Consequently, these un-sintered films failed to establish a continuous conductive network, making it impossible to obtain reliable resistance values using the four-point probe. In contrast, the PLS-treated composite formed a robust and uniform film that produced significantly larger and more consistent resistance shifts upon ESAT-6 exposure (Fig. S1). These results confirm that PLS is the decisive factor for ensuring the mechanical integrity and electrical percolation of the sensing matrix, thereby enhancing both sensitivity and reproducibility. Morphological analysis further confirmed that the synergistic effect of PANI and PLS-induced sintering formed a more continuous and robust matrix compared to MOFs alone (Fig. S2). To optimize device architecture, three paper layouts were evaluated: paper #1 (with buffer zone), paper #2 (without buffer zone), and paper #3 (non-microfluidic). Paper #3 exhibited excessive variability due to interferent accumulation, whereas paper #2 suffered from instability caused by Nafion solution diffusion into the detection zone (Fig. 1a). Paper #1, incorporating a buffer zone, effectively prevented Nafion infiltration and demonstrated superior stability. ELISA validation further confirmed efficient antigen transport in paper #1, yielding the strongest absorbance peak at 450 nm (Fig. 1b).

Electrochemically-based biosensor

In CV analysis, pure MOFs showed weak signals, while PANI yielded strong baseline currents due to high conductivity (Fig. 1c). The MOF–PANI composite showed intermediate conductivity but exhibited the largest signal changes upon ESAT-6 binding, especially when further functionalized with antibodies via EDC-NHS chemistry (Fig. 1d). These findings highlight the synergistic benefits of combining MOFs and PANI for electrochemical sensing.

Characterization

Paper-based biosensor

The surface morphology of each modification step in the $(Cu–S)_n$ MOF–PANI paper-based biosensor is shown in Fig. 2a After xenon PLS, the $(Cu–S)_n$ MOF–PANI composite displayed porous structures. Following EDC-NHS activation, the surface became denser with smoother edges. Subsequent covalent immobilization of Ab on the activated surface resulted in the appearance of nano-sized granular features. After blocking nonspecific sites with BSA, additional spherical deposits were observed, with some pores partially filled. Finally, binding of the ESAT-6 antigen produced protrusions and a visibly thicker coating layer, confirming successful antigen attachment on the $(Cu–S)_n$ MOF–PANI matrix.

Control SEM images of unsintered PANI, $(Cu–S)_n$ MOFs, and the composite (Fig. S2c-e) revealed marked differences from the sintered material. Pulsed xenon light treatment fused the components into a more continuous porous network, as reflected in the enhanced morphological integrity of the composite. Importantly, this PLS-induced structural refinement correlates directly with the superior sensing performance observed in Fig. S1, as the continuous network facilitates more efficient charge transfer and provides a more stable platform for analyte interaction compared to its unsintered counterpart.

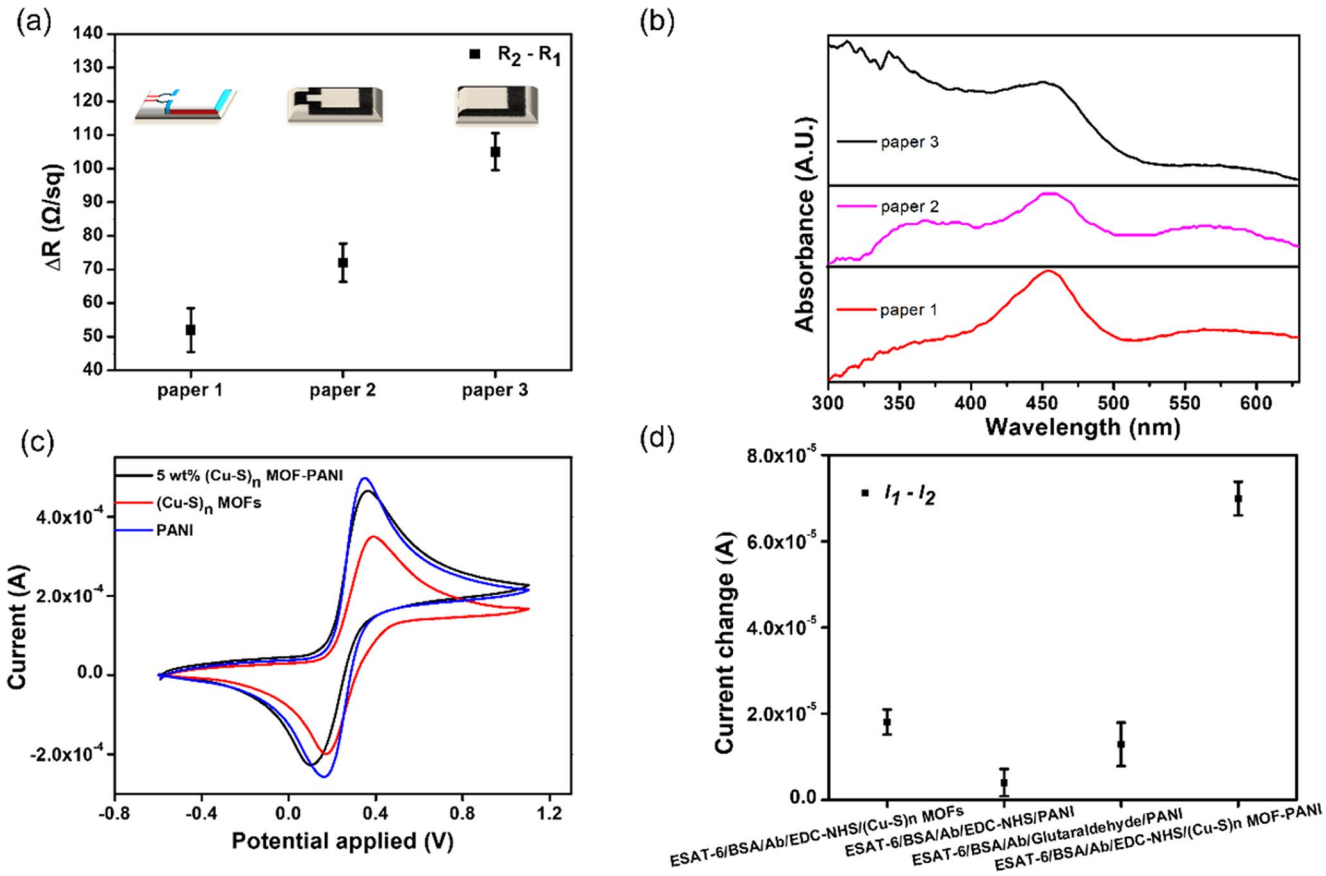

Fig. 1 (**a**) ΔR responses of ESAT-6 detected by three paper-based microfluidic sensing platforms (paper #1–3). (**b**) UV–Vis absorption spectra of the treated papers (paper #1–3). (**c**) CV of electrodes modified with different materials. (**d**) Comparison of the change in oxidation peak current upon ESAT-6 (0.39 nM) addition using different electrode materials. The y-axis represents the relative change in oxidation peak current ($\Delta I = I_1 - I_2$), where I_1 denotes the oxidation peak current obtained from PBS/BSA/Ab/crosslinker/base material, and I_2 denotes the oxidation peak current after ESAT-6/BSA/Ab/crosslinker/base material modification

Electrochemically-based biosensor

The surface morphology of electrodes modified with different materials was analyzed by SEM at 3,000× magnification (Fig. 3a). For morphological characterization, all samples were deposited onto indium tin oxide (ITO) glass substrates prior to SEM imaging. PANI/GCE displayed a uniform fibrous network that covered the electrode surface, consistent with the conductive framework of the polymer (Fig. S3 In contrast, $(Cu–S)_n$ MOFs/GCE exhibited a layered sheet-like architecture with high surface area, confirming successful MOFs deposition. The $(Cu–S)_n$ MOF–PANI composite, prepared by camphorsulfonic acid dispersion and centrifugation, showed smaller MOFs domains evenly distributed on the GCE surface, forming a more homogeneous and stable coating that supported reproducible electrochemical performance. The different rotational speeds result in different surface morphologies, as shown in Fig. S2c-e and Fig. S3 plot.

Stepwise surface functionalization further modified the composite morphology (Fig. 3a). Following EDC-NHS activation, a thin continuous layer enveloped the MOF–PANI surface. Antibody immobilization introduced granular and columnar features, consistent with protein attachment. Subsequent BSA blocking produced a thicker and smoother layer, partially covering surface pores and irregularities, thereby minimizing nonspecific binding. Finally, after ESAT-6 antigen binding, pronounced protrusions and localized agglomerates were observed, reflecting antigen–antibody interactions and confirming the successful capture of ESAT-6 on the electrode surface.

Surface chemical characterization

To confirm the chemical composition and the stepwise biomolecular functionalization, ATR–FTIR and XPS analyses were performed for both platforms.

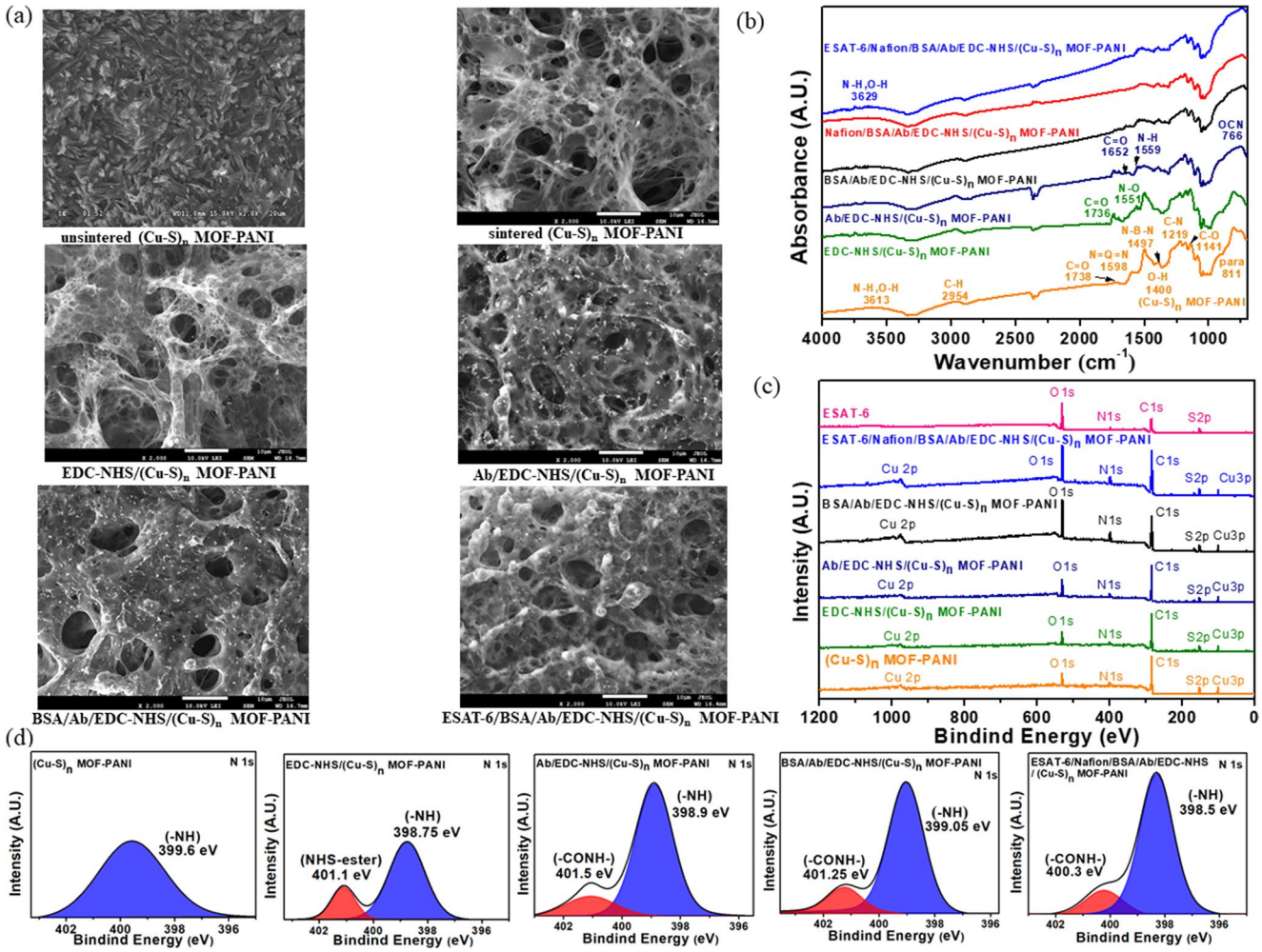

Fig. 2 (**a**) SEM images showing each step of surface modification of the $(Cu–S)_n$ MOF–PANI–based biosensor in the paper-based platform at 2,000× magnification. (**b**) ATR–FTIR spectra corresponding to each modification step. (**c**) XPS survey (wide-scan) spectra of the modified samples. (**d**) High-resolution XPS spectra of the N 1 s region, highlighting the chemical-state changes associated with surface functionalization

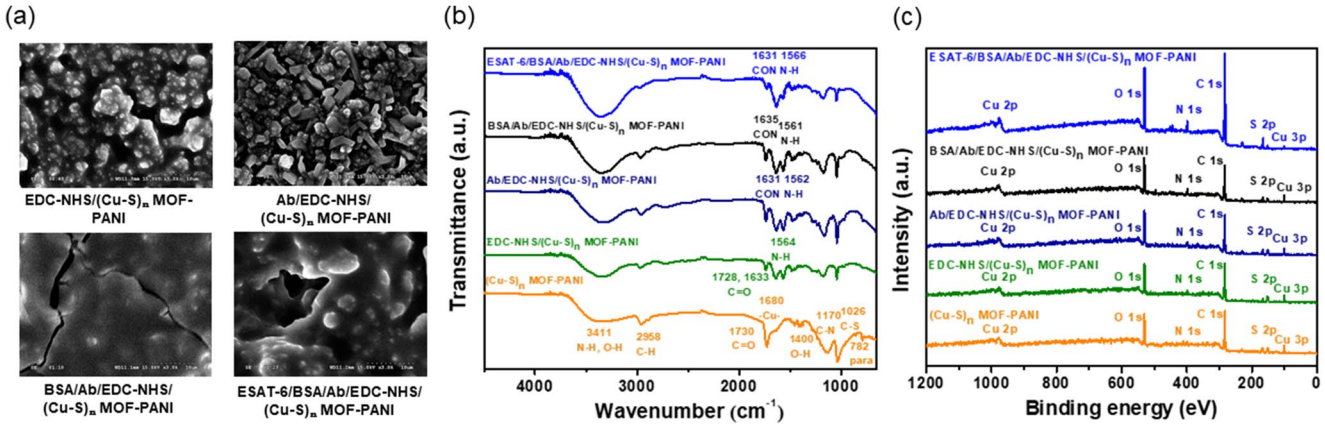

Fig. 3 (**a**) SEM images showing each step of surface modification of the electrochemically based $(Cu–S)_n$ MOF–PANI biosensor. (**b**) ATR–FTIR transmittance spectra corresponding to each modification stage. (**c**) XPS survey (wide-scan) spectra of the modified electrodes

Comparative FTIR analysis of sensing interfaces

The ATR–FTIR spectra of the paper-based biosensor after PLS (Fig. 2b, Fig. S4 and S5) and the unsintered electrochemical biosensor (Fig. 3b) were analyzed.

The PLS treatment significantly enhanced interfacial interactions, evidenced by the intensification of the C=O stretching band at 1738 cm^{-1} and the emergence of a Cu–π interaction peak at 811 cm^{-1}. These features indicate a strengthened coordination interaction between the MOF nodes and the PANI backbone induced by photothermal effects.

In contrast, the electrochemical sensor preserved the native vibrational features of the $(Cu–S)_n$ MOF–PANI hybrid (Fig. 3b), such as the N–H/O–H stretching at 3411 $cm^{-1}$and ligand coordination features at 1680 cm^{-1}, confirming the stability of the composite without thermal processing.

For both platforms, the subsequent bio-functionalization followed a consistent spectral evolution. The EDC-NHS activation was validated by the appearance of amide-related bands (Amide I and II) around 1633–1652 cm^{-1} and 1551–1564 cm^{-1}. Successful antibody conjugation and BSA blocking were corroborated by the pronounced enhancement of these amide features. Upon ESAT-6 introduction, specific antigen-antibody recognition was confirmed by further intensity shifts in the amide and N–H regions (3629 cm^{-1} for paper-based; relative intensity increase for electrochemical), signifying successful protein assembly on both modified surfaces.

XPS surface validation

XPS survey spectra (Figs. 2c and 3c) corroborated the hybrid composition, showing characteristic signals of C, O, N, S, and Cu for both sensors. The pulsed-light-treated surface exhibited larger signals in N 1 s and O 1 s following functionalization, suggesting a more active surface for protein binding. Conversely, the unsintered material showed a more gradual increase in N 1 s and O 1 s intensities, reflecting a progressive protein incorporation. High-resolution N 1 s spectra for both platforms revealed a distinct component at ~401.1 eV after activation, confirming the formation of NHS esters and subsequent covalent coupling of antibodies. These results collectively verify that while the initial material state (sintered vs. unsintered) differs, both platforms support robust and specific bio-functionalization for ESAT-6 detection.

Optimization of experimental conditions

To maximize the analytical performance and reproducibility of both biosensing platforms, fabrication and operational parameters were systematically optimized. (Fig. S6 and Fig. S7).

Shared material and buffer parameters

The $(Cu–S)_n$ MOF–PANI composite exhibited consistent optimal behavior across both platforms. A MOF loading of 5 wt% was selected as it provided the highest conductivity and most robust electron-transfer current, while 16 wt% CSA was found to be the optimal dopant concentration for maximizing PANI protonation. These standardized formulations, validated by the consistent baseline resistance (Fig. S6a) and oxidation peak current (Fig. S7a) across three independent synthesis lots (inter-batch RSD < 11%), demonstrate the high reproducibility and scalability of the fabrication process. Regarding the sensing environment, 10 mM PBS at pH 7.0 was identified as the ideal buffer. Higher pH levels (> 7.0) were found to impair the binding affinity or potentially denature the ESAT-6 antigen, while increased PBS concentrations led to undesirable background resistance or ionic interference.

Platform-specific optimizations

Photonic sintering was critical for the resistive interface in paper-based sensor. The optimal energy was determined to be 2400 J/cm^2 with eight pulses, which minimized substrate resistance while maintaining film integrity. For bio-functionalization, a 15 min EDC-NHS activation and 60 min antibody incubation (0.2 mg/mL) yielded the most stable resistance change (ΔR).

The coating volume and drying time were found to be pivotal for film stability on GCE. A 5 µL coating volume with a 9 min air-drying duration produced the most reproducible peak currents. Notably, the electrochemical platform demonstrated rapid recognition kinetics, with the antigen-antibody binding signal reaching a plateau within 2 min, significantly faster than the paper-based resistive response.

Functionalization efficiency

Both sensors shared an optimal EDC-NHS activation time of 15 min. For the antibody-antigen interaction, the paper-based system required higher volumes (5 µL) to ensure uniform coverage of the cellulose fibers, whereas the electrochemical GCE surface was effectively functionalized with 7 µL of antibody solution. These optimized conditions collectively ensured the high sensitivity and low LOD observed in subsequent clinical matrix evaluations.

Analytical performance of the ESAT-6 biosensor

Paper-based biosensor

The analytical performance of the paper-based biosensor was evaluated under optimized conditions, where increasing

ESAT-6 concentrations progressively impaired the conductivity of the composite sensing layer, resulting in a corresponding increase in electrical resistance. The LOD, based on a signal-to-noise ratio of 3, was determined to be 39.2 pM (1.32 ng/mL). As shown in Fig. S8, the biosensor displayed a strong linear response from a functional limit of quantification (LOQ) of 195 pM to a upper limit of quantification (ULOQ) of 50 nM (6.60–1.69×10^3 ng/mL), following the regression equation y = (35.13 ± 1.085) log[ESAT-6] – (80.65 ± 3.683) with an excellent correlation coefficient (R^2 = 0.994).

Compared with previously reported paper-based biosensors for tuberculosis biomarkers such as ESAT-6 (Table 1), the present system provides a wider linear range, lower LOD, and smaller required sample volume, making it suitable for quantifying blood plasma ESAT-6 levels in patients with active tuberculosis [15], [16] and [17].

Electrochemically-based biosensor

The electrochemical biosensor was evaluated by CV using the $[Fe(CN)_6]^{3-/4-}$ redox system. The stepwise surface modification of the sensor is illustrated in Fig. S9. As successive functional layers were introduced onto the electrode surface, a progressive decrease in the oxidation peak current was observed. Notably, ESAT-6 is an organic protein molecule, and its immobilization and increasing concentration

Table 1 Comparative performance summary of the two developed biosensing platforms and recently reported ESAT-6 sensors from other research groups

Paper-Based Biosensor

No.	Material	Detection platform	Sample	Volume (µL)	Detection method	Linear range (ng/mL)	Detection limit (ng/mL)	Ref.
1	[a]FND	[b]SELFIA	sputum	50	Fluorescence	0–10^3	2.00×10^{-2}	[15]
2	[c]AuNP	[d]LFIA	recombinant antigens (in PBS)	65	Colorimetric detection	[e]N.A.	6.25×10^{-2}	[16]
3	Gold	Screen-Printed Gold Electrode	culture filtrates proteins (in PBS)	50	[f]SWV	10–10^3	7.00	[17]
4	$(Cu–S)_n$ MOF–PANI	µPAD	blood plasma	5	Resistance method	6.60–1.69×10^3	1.32	present work

Electrochemically-Based Biosensor

No.	Material	Detection platform	Sample	Volume (µL)	Detection method	Linear range (ng/mL)	Detection limit (ng/mL)	Ref.
1’	[a’]N-GO	GCE	serum	[e]N.A.	[b’]EIS	$10^{-2} – 10^2$	7.00×10^{-3}	[18]
2’	[c’]MXene/C_{60}NPs/Au@Pt	GCE	serum	10	[d’]DPV, [e’]IT	$10^{-4} – 5 \times 10$	2.88×10^{-6} (DPV) 1.35×10^{-5} (IT)	[19]
3’	[f’]$Ti_3C_2T_x$	GCE	serum	20	DPV	$10^{-5} – 10^2$	4.07×10^{-6}	[20]
4’	[g’]N-CNTs-Au	GCE	serum	[e]N.A.	CV, EIS	$10^{-4} – 5 \times 10$	2.36×10^{-6}	[21]
5’	[h’]Ni-rGO-PANI	Ni-rGO-PANI metal carbon-polymer composite film	blood plasma	1000	CV	1.0–10^2	1.04	[22]
6’	[i’]NG@Zr-MOF-on-Ce-MOF@Tb	GCE	serum	20	CV	$10^{-4} – 10$	1.20×10^{-5}	[23]
7’	[j’]NiMn-LDHs@PdNPs	GCE	serum	[e]N.A.	CV	$7.5 \times 10^{-4} – 10$	6.29×10^{-4}	[24]
8’	[k’]PEDOT-COOH	Gold Electrode	blood plasma	5	CV	$8.1 \times 10^{-1} – 1.69 \times 10^3$	4.70×10^{-2}	our previous work, [25]
9’	$(Cu–S)_n$ MOF–PANI	GCE	artificial urine	5	CV	$7.99 \times 10^{-4} – 5.28 \times 10$	5.68×10^{-5}	present work

[a]FND: Fluorescent nanodiamond. [b]SELFIA: Spin-enhanced lateral flow immunoassay. [c]AuNP: gold nanoparticle. [d]LFIA: Lateral flow immunoassay. [e]N.A.: Not Available. [f]SWV: Square wave voltammetry. [a’]N-GO: N-doped graphene oxide. [b’]EIS: Electrochemical Impedance Spectroscopy. [c’]MXene/C60NPs/Au@Pt: Mxene a novel type of metal carbides and nitrides material. C_{60}NPs: Fullerence nanoparticles. Au@Pt: Core-shell bimetallic Au@Pt nanostructures. [d’]DPV: Differential Pulse Voltammetry. [e’]IT: Amperometric i-t curves. [f’]$Ti_3C_2T_x$: Titanium carbide. [g’]N-CNTs-Au: Gold nanoparticles supported nitrogen-doped carbon nanotube. [h’]Ni-rGO-PANI: Ni nanoparticles/reduced Graphene oxide/polyaniline. [i’]NG@Zr-MOF-on-Ce-MOF@Tb: Nitrogen-doped graphene/Zr-MOF-on-Ce-MOF/Toluidine Blue nanohybrid. [j’]NiMn-LDHs@PdNPs: NiMn-layered double hydroxides@palladium nanoparticles. [k’]PEDOT-COOH: poly(3,4-ethylene dioxythiophene) with carboxyl groups.

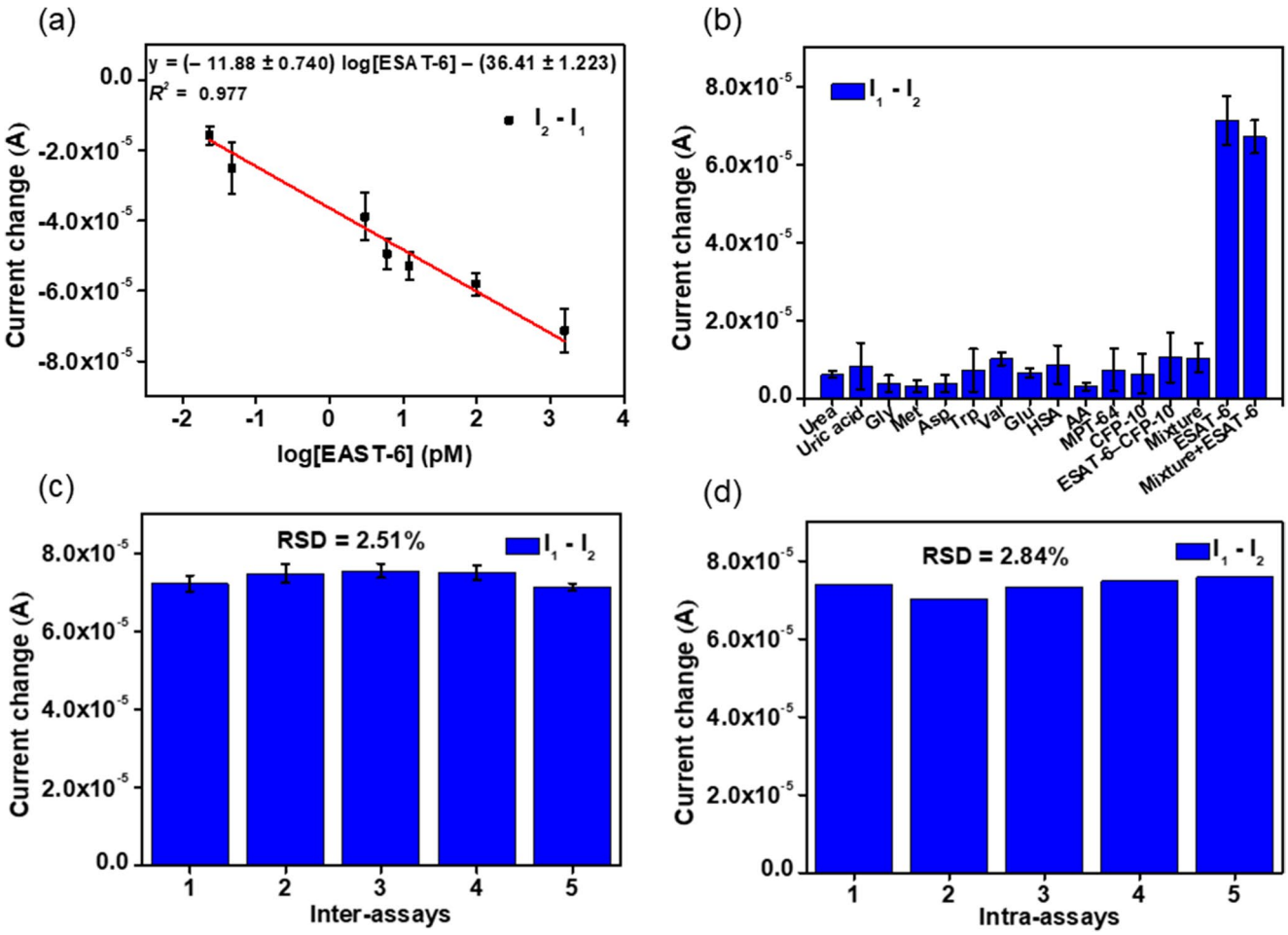

Fig. 4 Analytical performance of the electrochemical biosensor for ESAT-6 detection. (**a**) Calibration curve of oxidation peak current change (ΔI) versus log[ESAT-6] ($n=3$). (**b**) Interference assessment using common urinary components (900 µg/mL urea, 1.5 µg/mL uric acid, 900 µg/mL Gly, 0.056 µg/mL Met, 0.1 µg/mL Asp, 0.159 µg/mL Trp, 0.293 µg/mL Val, 36 µg/mL Glu, 3.75 µg/mL HSA, 2.5 µg/mL AA) and tuberculosis-related proteins (29.5 nM MPT-64, CFP-10, ESAT-6–CFP-10 hybrid). A mixed solution containing all interferents (Mixture) and the same mixture with 1.56 nM ESAT-6 (Mixture + ESAT-6) were also tested ($n=3$). (**c**) Inter-assays repeatability was measured using 1.56 nM ESAT-6 ($n=3$). (d) Intra-assay reproducibility over 5 consecutive days was measured using 1.56 nM ESAT-6

further hindered electron transfer between the redox couple and the electrode surface, resulting in a gradual attenuation of the CV current response.

As shown in Fig. 4a, I_1 represents the oxidation peak current of the functionalized electrode in PBS, whereas I_2 corresponds to the current after exposure to ESAT-6. The difference ($\Delta I = I_2 - I_1$) reflects the signal change induced by antigen binding. A linear correlation was obtained between ΔI and the logarithm of ESAT-6 concentration over the range of 23.6 fM–1.56 nM ($7.99\times10^{-4} - 5.28\times10^{1}$ ng/mL), following the equation y = (– 11.88 ± 0.740) log[ESAT-6] – (36.41 ± 1.223) (R^2= 0.977). The LOD was 1.68 fM (5.68×10^{-5} ng/mL), demonstrating ultrasensitive performance at the femtomolar level.

Compared with previously reported electrochemical biosensors for detecting tuberculosis-associated biomarkers (Table 1), our developed platform demonstrated superior analytical performance, characterized by a lower detection range, lower LOD, and reduced sample volume. Furthermore, the platform's unique advantage in using artificial urine as a detection matrix highlights its potential for noninvasive tuberculosis diagnosis. In previous studies, the concentration of ESAT-6 detected in urine samples from most non-tuberculosis patients was below the limit of detection (6 pg/mL = 6×10^{-3} ng/mL), clearly distinguishing infected from non-infected individuals [26]. In the present work, the detection range of our biosensor covers the clinically relevant ESAT-6 concentrations found in both TB-positive and TB-negative subjects, demonstrating its potential for differentiating disease status through urine-based detection. The integration of a MOF–polymer composite electrode contributed to the remarkably low LOD and minimal sample volume requirement, outperforming comparable electrochemical sensors reported previously.

Selectivity and interference evaluation

To evaluate analytical specificity within complex biological matrices, both platforms were challenged with potential interferents. For the blood plasma-based (paper) sensor, common components (AA, Glu, HSA) and TB-specific proteins (CFP-10, MPT-64) were examined, while the urine-based (electrochemical) sensor was tested against urea, uric acid, and various amino acids (Gly, Met, Asp, Trp, Val).

To suppress inherent matrix effects and high ionic backgrounds, samples were diluted—40-fold for artificial urine and 25-fold for blood plasma—following optimized analytical workflows. Despite these dilutions, interferent concentrations remained several orders of magnitude higher than the target ESAT-6, the $(Cu–S)_n$ MOF–PANI sensing interface maintained high accuracy, demonstrating the robust anti-interference capability of the composite. A critical distinction emerged during the comparative evaluation of the ESAT-6–CFP-10 heterodimer (Figs. 4b and 5a). The paper-based sensor exhibited partial cross-reactivity toward this complex. This broad-spectrum recognition is analytically advantageous for initial screening, as it captures both free ESAT-6 and its hybrid forms. This response likely stems from the porous cellulose matrix, which facilitates different orientations or non-specific interactions of the heterodimer, despite partial epitope masking [16].

In contrast, the GCE-based electrochemical sensor demonstrated superior molecular specificity by effectively suppressing signals from the ESAT-6–CFP-10 complex. This high tolerance suggests that the electrochemical interface, governed by direct electron-transfer kinetics, is more sensitive to the precise steric configuration of the antigen. Consequently, the electrochemical platform is better suited for the highly selective quantification of free ESAT-6.

Precision and long-term stability

The reproducibility of the dual platforms was validated through intra- and inter-assay precision tests (Figs. 4c-d and 5b-c). Both systems demonstrated high precision; the paper-based sensor yielded RSDs below 4%, while the electrochemical sensor showed superior precision with RSDs below 3.5% over five consecutive days. Regarding long-term robustness, the paper-based biosensor exhibited a remarkable shelf-life, maintaining a stable response within ± 4% RSD after 32 days of storage at 4 °C. Similarly, the electrochemical platform demonstrated robust storage stability, retaining 95.8% of its initial response after 12

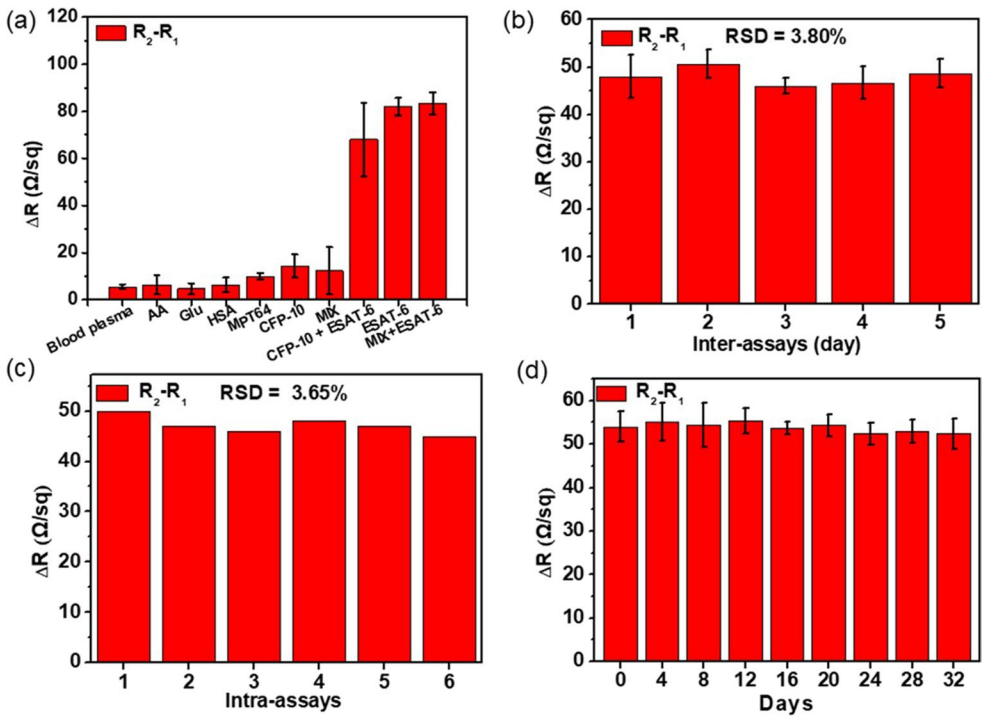

Fig. 5 Analytical performance of the paper-based biosensor for ESAT-6 detection. (**a**) Interference assessment with common blood plasma components (0.014 mg/mL AA, 1.8 mg/mL Glu, 5 mg/mL HSA), tuberculosis-related proteins (3.125 mg/mL CFP-10, 0.366 mg/mL MPT-64, 3.125 nM ESAT-6–CFP-10 hybrid, and 50 nM ESAT-6), and a mixed solution containing all interferents with ESAT-6 ($n=3$). (**b**) Inter-assay repeatability for 4.78 nM ESAT-6 over five consecutive days ($n=3$). (**c**) Intra-assay repeatability for 4.52 nM ESAT-6. (d) Storage stability of the biosensor evaluated over 32 days using 7.01 nM ESAT-6 ($n=3$)

days (Fig. S10). These results confirm that the $((Cu–S)_n$ MOF–PANI composite provides a stable and reliable sensing interface, suitable for both rapid point-of-care screening (paper-based) and high-sensitivity quantitative diagnostics (electrochemical).

Spiked recovery experiment

Methodological strategy and recovery rationale

To systematically evaluate the methodological recovery and matrix effects, spiked samples were utilized—a standard and rigorous strategy for disease-associated biomarkers like ESAT-6 that are absent in healthy biofluids. To ensure the highest analytical fidelity, the ESAT-6 antigen was spiked into undiluted human blood plasma and artificial urine at the beginning of the workflow, followed by the respective dilution protocols. This approach confirms the sensors' ability to handle complex biological matrices during the initial recognition stage. Furthermore, to confirm the complementary utility of the two platforms, a cross-platform validation was conducted in a shared blood plasma matrix, ensuring that the superior sensitivity of the electrochemical method and the rapid screening capability of the paper-based platform can be reliably integrated into a unified diagnostic framework.

Performance in human blood plasma (paper-based sensor)

The quantitative reliability of the resistance-based sensor was validated across a concentration range encompassing the reported clinical threshold for tuberculosis (1.05×10^2 ng/mL). To ensure analytical fidelity, undiluted blood plasma samples were first spiked with ESAT-6 and subsequently diluted 25-fold with 10 mM PBS (pH 7.0), yielding final test concentrations from 26.2 to 1693.5 ng/mL (0.78 to 50 nM). As summarized in Table 2, the recovery values ranged from 92.9% to 101.0% with RSDs between 1.86% and 4.12%. The high degree of accuracy and reproducibility underscores the potential of this paper-based platform as a robust tool for rapid blood plasma-based screening. These results were further benchmarked against a commercial ELISA kit.

Performance in artificial urine (electrochemical sensor)

To demonstrate the matrix tolerance of the $(Cu–S)_n$ MOF–PANI composite in non-invasive diagnostics, recovery experiments were conducted in artificial urine, focusing on both trace-level and disease-relevant regimes. Following the established protocol, raw artificial urine was spiked with ESAT-6 and then subjected to a 40-fold total dilution to mitigate ionic interference while maintaining detectable analyte levels. The final test concentrations ranged from 7.99×10^{-4} to 52.84 ng/

Table 2 Recovery results of ESAT-6 in samples determined by two biosensor platforms: Paper-based biosensor ESAT-6 recovery test results using resistance method and ELISA methods in human blood plasma ($n = 3$). Electrochemically-based biosensor recovery results of ESAT-6 determined by the CV method in artificial urine samples ($n = 5$)

Paper-Based Biosensor

Sample	Added ESAT-6 (ng/mL)	measured by the resistive method (ng/mL)	Recovery (%)	RSD (%)	ELISA method (ng/mL)	Recovery (%)	RSD (%)
1	2.62×10^1	$(2.44 \pm 0.05) \times 10^1$	92.9	2.18	-[a]		
2	5.28×10^1	$(5.35 \pm 0.16) \times 10^1$	101.0	3.02	$(5.54 \pm 0.06) \times 10^1$	105.0	1.16
3	9.97×10^1	$(9.71 \pm 0.18) \times 10^1$	97.4	1.86	$(1.03 \pm 0.09) \times 10^2$	103.0	8.45
4	8.45×10^2	$(8.08 \pm 0.26) \times 10^2$	95.6	3.16	-[a]		
5	1.69×10^3	$(1.58 \pm 0.07) \times 10^3$	93.5	4.12	$(1.59 \pm 0.18) \times 10^3$	94.5	11.5

Electrochemically-Based Biosensor

Sample	Added ESAT-6 (ng/mL)	CV method (ng/mL)	Recovery (%)	RSD (%)	ELISA method (ng/mL)	Recovery (%)	RSD (%)
1'	7.99×10^{-4}	$(7.84 \pm 0.29) \times 10^{-4}$	98.1	3.67	-[b]		
2'	1.28×10^{-2}	$(1.31 \pm 0.10) \times 10^{-2}$	103.0	4.58			
3'	2.05×10^{-1}	$(1.93 \pm 0.10) \times 10^{-1}$	94.0	4.24			
4'	3.29	3.39 ± 0.17	103.0	4.87			
5'	5.28×10^1	$(5.04 \pm 0.16) \times 10^1$	95.4	3.20			

-: not detected

[a] See the section on the Comparison between Paper-Based Sensors and ELISA Kits

[b] Out of the detection range of ELISA.

mL (23.6 fM to 1.56 nM). The electrochemical platform exhibited exceptional accuracy, with recovery values of 94.0% to 103.0% and RSDs between 3.20% and 4.87% ($n=5$). Direct benchmarking against ELISA for concentrations below 1.56 ng/mL (52.8 ng/mL) was not feasible due to the kit's sensitivity threshold. However, at the overlapping concentration of 1.56 nM (52.84 ng/mL) in a diluted blood plasma matrix, the electrochemical platform showed results highly consistent with the ELISA benchmark (95.6% vs. 105.0% recovery). Given that blood plasma is a more chemically complex biological matrix than artificial urine, this cross-matrix consistency validates the methodological accuracy and robustness of the $(Cu–S)_n$ MOF–PANI platform. Consequently, the high recovery rates obtained in artificial urine (94.0%−103.0%) can be considered reliable for subsequent ultra-trace quantification in clinical contexts.

Cross-platform validation and synergistic analysis

To validate the complementary performance of the two sensing strategies, a head-to-head comparison was conducted in a shared blood plasma matrix. A concentration of 1.56 nM (52.8 ng/mL) was selected as the cross-validation point, as it falls within the operational linear range of both platforms. To minimize matrix effects and non-specific protein adsorption during electrochemical analysis, the spiked plasma samples were diluted 100-fold with pH 7.4 PBS prior to measurement. As summarized in Table S1, the paper-based sensor and the electrochemical platform yielded highly consistent recovery values of 101.0% and 95.6%, respectively. Crucially, these results were further benchmarked against a commercial ELISA kit, which showed a comparable recovery of 105.0% at the same concentration. The high degree of correlation among the three methods confirms the accuracy of our platforms. This synergistic approach ensures that the diagnostic framework can provide ultra-sensitive detection at the femtomolar level while maintaining the capability for rapid, cost-effective screening at higher clinical concentrations, offering a comprehensive solution for tuberculosis monitoring.

Comparative analytical summary

The successful recovery across both matrices—spanning from femtomolar levels in urine to nanomolar levels in blood plasma—demonstrates the versatility and robustness of the dual-platform sensing strategy. By leveraging the same conductive composite, the paper-based sensor provides a rapid response optimized for clinical thresholds, while the electrochemical sensor offers the extreme sensitivity required for early-stage or non-invasive detection. Collectively, these complementary systems provide a comprehensive and reliable solution for ESAT-6 monitoring in diverse biological environments.

Discussion: comparative analysis of sensing architectures

The dual-platform strategy developed in this study leverages the unique properties of the $(Cu–S)_n$ MOF–PANI composite to meet diverse clinical diagnostic needs. The distinct sensing behaviors observed between the paper-based microfluidic and electrochemical platforms arise from fundamental differences in their interfacial physics and signal transduction mechanisms.

Sensitivity and transduction efficiency

The electrochemical platform achieves an ultra-low fM-level LOD, primarily due to the direct electron transfer between the $(Cu–S)_n$ MOF–PANI layer and the GCE, which minimizes interfacial resistance. In contrast, the paper-based platform operates via capillary-driven flow within a 3D porous matrix. While this architecture facilitates rapid sample transport, the passive mass transport and increased background noise limit its sensitivity to the pM range. Interestingly, the electrochemical system requires more precise surface equilibration, whereas the paper-based system offers a broader dynamic range suitable for high-concentration blood plasma screening.

Selectivity and matrix interference

The distinct interference tolerance of the two platforms was experimentally validated. The paper-based sensor showed partial cross-reactivity toward the ESAT-6–CFP-10 heterodimer (Fig. 5), likely due to the high surface-area-to-volume ratio of the cellulose network (Fig. S2) promoting multi-epitope interactions. While this reduces molecular specificity, it is clinically advantageous for broad TB screening. In contrast, EIS analysis (Fig. S11) confirmed the electrochemical platform's high specificity. The substantial increase in R_{ct} for free ESAT-6 versus negligible change for the heterodimer demonstrates that the electrochemical interface effectively discriminates against the bulkier complex via steric exclusion. This physical hindrance at the $(Cu–S)_n$ MOF–PANI surface ensures superior precision for ultra-trace quantification.

Clinical utility and complementarity

The two platforms offer complementary operational advantages The paper-based system excels in portability, cost-effectiveness, and rapid processing, making it an ideal candidate for POCT in resource-limited settings. The electrochemical system, while requiring more sophisticated instrumentation, provides the extreme precision necessary for non-invasive

diagnostics. By integrating both platforms, this study provides a comprehensive diagnostic solution that covers the entire spectrum of clinical TB monitoring, from rapid field screening to high-sensitivity clinical quantification.

Comparison between paper-based sensors and ELISA kits

The proposed sensor's performance was benchmarked against a commercial ELISA kit (linear range: 1.56–100 ng/mL). To ensure compatibility, samples at 845 ng/mL were diluted to 21.12 ng/mL. However, experimental results revealed poor RSD and increased error at concentrations near 21.12 and 26.2 ng/mL (Table 2), indicating that the kit's precision is compromised at these lower concentrations. Nevertheless, for samples within the reliable detection range of the ELISA kit (Samples 2, 3, and 5), the results from our paper-based sensor showed an excellent linear correlation ($R^2 = 0.9999$) and no significant statistical difference ($p > 0.05$) compared to the reference technique, validating the platform's analytical accuracy. These results highlight the inherent limitations of ELISA: it is not only time-consuming (4-hour process) and labor-intensive but also prone to performance fluctuations at the lower end of its scale. Our paper-based platform addresses these issues by offering superior precision and operational simplicity, making it a more reliable solution for ESAT-6 detection.

Reliability and anti-fouling performance in complex matrices

To address potential signal drift and sensor fouling in complex biofluids, both platforms were developed as disposable, single-use devices, ensuring that each measurement is performed on a pristine interface. For the paper-based sensor, a Nafion membrane was integrated to act as an anti-fouling layer, effectively isolating non-specific components in blood plasma. Furthermore, the accuracy of each session is maintained through daily calibration curves and, for the paper platform, a four-point probe resistance calibration. The robustness of these strategies is supported by the interference studies in Figs. 4 and 5, which confirm the sensors' high fidelity in both urine and plasma matrices without the influence of bio-fouling.

Practicality and scalability

The dual-platform strategy offers significant advantages in scalability and clinical utility. High-speed processing (millisecond-range) enables high-throughput, roll-to-roll manufacturing of the sensing interfaces. By utilizing a direct sensing mechanism, we eliminate expensive secondary antibodies and enzymatic kits, reducing material costs to approximately 5–10 USD per test. Furthermore, the use of a portable four-point probe instrument ensures precise resistance readout in field settings. Compared to traditional sputum culture, the use of blood plasma and urine enhances safety and patient compliance, providing a robust and accessible solution for tuberculosis monitoring in resource-limited environments.

Limitations of the work

Although this study demonstrates the high performance and reproducibility of the dual sensing platforms, several limitations provide a roadmap for future development. First, while high recovery was achieved in spiked biofluids, further validation with a larger cohort of diverse clinical samples from tuberculosis patients is essential to confirm diagnostic accuracy in real-world settings. Furthermore, extending shelf-life evaluation to commercial standards (e.g., beyond six months) and optimizing mass-production variables—specifically the PLS sintering and MOF loading processes during the transition from laboratory-scale to automated synthesis—remain critical steps for successful commercial translation.

Conclusions

In conclusion, we have demonstrated a versatile dual-biosensing strategy for the detection of the ESAT-6 biomarker, leveraging the synergistic properties of a $(Cu–S)_n$ MOF–PANI conductive composite. A significant aspect of this work is the application of pulsed light sintering, which modulates the composite's conductivity and surface chemistry to enable effective sensing across two distinct architectures. The paper-based microfluidic resistive sensor provides a cost-effective and rapid screening tool for blood plasma samples, covering the clinically relevant nanomolar range. Complementing this, the electrochemical GCE-based biosensor achieves an ultralow femtomolar-level detection limit (23.6 fM), offering the extreme sensitivity required for non-invasive urine diagnostics. Our findings, validated in spiked human blood plasma and artificial urine, show that this integrated approach provides a complementary framework for both rapid screening and high-precision quantification. While further clinical validation with patient-derived samples is necessary, this dual-platform methodology, enabled by MOF-polymer engineering, offers a promising and potentially scalable solution for the early diagnosis and monitoring of tuberculosis, particularly suited for diverse clinical and resource-limited settings.

Supplementary Information The online version contains supplementary material available at https://doi.org/10.1007/s00604-026-08007-5.

Acknowledgements The authors are grateful to Ms. S.-J. Ji for her assistance in the SEM experiments.

Author contributions P.-H. Chiang, Z.-R. Liang, Y.-H. Lu, S.-H. Chen, and R.-T. Tang carried out sensor preparation and experimental analysis. Y.-H. Yu designed and synthesized the MOF materials. M.-L. Ho conceived and designed the experiments and prepared the original draft of the manuscript. All authors have read and agreed to the published version of the manuscript.

Funding Open access funding provided by Fu Jen Catholic University. The research was supported by the National Science and Technology Council, Taiwan (Grant number 114-2113-M-030-009-).

Data availability No datasets were generated or analysed during the current study.

Declarations

Competing interests The authors declare no competing interests.

References

1. Chakaya J, Khan M, Ntoumi F, Aklillu E, Fatima R, Mwaba P, Kapata N, Mfinanga S, Hasnain SE, Katoto PD (2021) Global Tuberculosis Report 2020–Reflections on the Global TB burden, treatment and prevention efforts. International journal of infectious diseases 113:S7–S12. https://doi.org/10.1016/j.ijid.2021.02.107
2. Yayan J, Franke K-J, Berger M, Windisch W, Rasche K (2024) Early detection of tuberculosis: a systematic review. Pneumonia 16:11. https://doi.org/10.1186/s41479-024-00133-z
3. Chauke SH, Nzuza S, Ombinda-Lemboumba S, Abrahamse H, Dube FS, Mthunzi-Kufa P (2024) Advances in the detection and diagnosis of Tuberculosis using optical-based devices. Photodiagnosis and photodynamic therapy 45:103906. https://doi.org/10.1016/j.pdpdt.2023.103906
4. Sun F, Li J, Cao L, Yan C (2024) Mycobacterium tuberculosis virulence protein ESAT-6 influences M1/M2 polarization and macrophage apoptosis to regulate tuberculosis progression. Genes & Genomics 46:37–47. https://doi.org/10.1007/s13258-023-01469-4
5. Salimiyan Rizi K, Aryan E, Meshkat Z, Ranjbar G, Sankian M, Ghazvini K, Farsiani H, Pourianfar HR, Rezayi M (2021) The overview and perspectives of biosensors and Mycobacterium tuberculosis: A systematic review. Journal of Cellular Physiology 236:1730–1750. https://doi.org/10.1002/jcp.30007
6. Deng L-E, Guo M, Deng Y, Pan Y, Wang X, Maduraiveeran G, Liu J, Lu C (2024) MOF-based platform for kidney diseases: advances, challenges, and prospects. Pharmaceutics 16:793. https://doi.org/10.3390/pharmaceutics16060793
7. Meskher H, Mustansar HC, Thakur AK, Sathyamurthy R, Lynch I, Singh P, Han TK, Saidur R (2023) Recent trends in carbon nanotube (CNT)-based biosensors for the fast and sensitive detection of human viruses: a critical review. Nanoscale advances 5:992–1010. https://doi.org/10.1039/D2NA00236A
8. Jeong S, Moon HR (2024) Metal–organic frameworks as a fluorescent probe for detection of pathogenic biomarkers in human urine. Bulletin of the Korean Chemical Society 45:308–316. https://doi.org/10.1002/bkcs.12827
9. Huang J, Pan J, Song Y, Lin Q, Xu Y, Dai Z, Liu S-Y (2024) MOF-functionalized paper-based biosensors: fabrications, mechanisms and applications. TrAC Trends in Analytical Chemistry 173:117619. https://doi.org/10.1016/j.trac.2024.117619
10. Huang D, Ma H, Wang J, Du Y, Li R (2024) Mof-mediated paper-based (bio) sensors for detecting of food and environmental pollutants: Preparation strategies and emerging applications. Microchemical Journal 207:111692. https://doi.org/10.1016/j.microc.2024.111692
11. Meskher H, Belhaouari SB, Sharifianjazi F (2023) Mini review about metal organic framework (MOF)-based wearable sensors: challenges and prospects. Heliyon. https://doi.org/10.1016/j.heliyon.2023.e21621
12. Meskher H, Ragdi T, Thakur AK, Ha S, Khelfaoui I, Sathyamurthy R, Sharshir SW, Pandey A, Saidur R, Singh P (2024) A review on CNTs-based electrochemical sensors and biosensors: unique properties and potential applications. Critical reviews in analytical chemistry 54:2398–2421. https://doi.org/10.1080/10408347.2023.2171277
13. Pathak A, Shen J-W, Usman M, Wei L-F, Mendiratta S, Chang Y-S, Sainbileg B, Ngue C-M, Chen R-S, Hayashi M (2019) Integration of a (–Cu–S–) n plane in a metal–organic framework affords high electrical conductivity. Nature communications 10:1721. https://doi.org/10.1038/s41467-019-09682-0
14. Yu Y-H, Lin X-Y, Teng K-L, Hu C-C, Wang W-Y, Hung Y-H, Tseng H-Y, Luo K-H, Yeh J-M, Lu K-L (2024) Semiconductive (Cu–S) n metal–organic frameworks hybrid polyaniline nanocomposites as hydrogen sulfide gas sensor. Surfaces and Interfaces 44:103698. https://doi.org/10.1016/j.surfin.2023.103698
15. Le T-N, Descanzo MJN, Hsiao W-W, Soo P-C, Peng W-P, Chang H-C (2024) Fluorescent nanodiamond immunosensors for clinical diagnostics of tuberculosis. Journal of Materials Chemistry B 12:3533–3542. https://doi.org/10.1039/D3TB03038E
16. Seele PP, Dyan B, Skepu A, Maserumule C, Sibuyi NRS (2023) Development of gold-nanoparticle-based lateral flow immunoassays for rapid detection of TB ESAT-6 and CFP-10. Biosensors 13:354. https://doi.org/10.3390/bios13030354
17. Diouani MF, Ouerghi O, Refai A, Belgacem K, Tlili C, Laouini D, Essafi M (2017) Detection of ESAT-6 by a label free miniature immuno-electrochemical biosensor as a diagnostic tool for tuberculosis. Materials Science and Engineering: C 74:465–470. https://doi.org/10.1016/j.msec.2016.12.051
18. Xia Y, Zhu H, Liu R, Li X, Xie X, Zhao J, Li J, Jiao X, Yang Z, Chen X (2023) Picogram level electrochemical impedimetric immunosensor for monitoring Mycobacterium tuberculosis based on specific and sensitive ESAT-6 monoclonal antibody. Talanta 253:124052. https://doi.org/10.1016/j.talanta.2022.124052
19. Huang H, Chen Y, Zuo J, Deng C, Fan J, Bai L, Guo S (2023) MXene-incorporated C60NPs and Au@ Pt with dual-electric signal outputs for accurate detection of Mycobacterium tuberculosis ESAT-6 antigen. Biosensors and Bioelectronics 242:115734. https://doi.org/10.1016/j.bios.2023.115734

20. Zuo J, Yuan Y, Qing M, Chen Y, Huang H, Zhou J, Bai L, Liang H (2024) Surface-Activated Ti3C2Tx Adsorption of Acetylene Black Coupled with Polyaniline as a Signal Tag for the Detection of the ESAT-6 Antigen of Mycobacterium tuberculosis. ACS Applied Materials & Interfaces 16:17300–17312. https://doi.org/10.1021/acsami.4c01593
21. Chen Y, Gu Y, Yi X, Huang H, Li Y, Yang B, Guo S, Bai L (2023) Conductive nano-gold self-assembled MXene@ hemin with high catalytic activity achieved by strong metal-support interactions: A powerful nanozyme for development of electrochemical aptasensor in tuberculosis diagnosis. Chemical Engineering Journal 466:143112. https://doi.org/10.1016/j.cej.2023.143112
22. Omar RA, Verma N, Arora PK (2021) Development of ESAT-6 based immunosensor for the detection of mycobacterium tuberculosis. Frontiers in Immunology 12:653853. https://doi.org/10.3389/fimmu.2021.653853
23. Xie J, Mu Z, Yan B, Wang J, Zhou J, Bai L (2021) An electrochemical aptasensor for Mycobacterium tuberculosis ESAT-6 antigen detection using bimetallic organic framework. Microchimica Acta 188:404. https://doi.org/10.1007/s00604-021-05058-8
24. Zhang Q, Zhou J, Chen Y, Gu Y, Yang J, Hu Q, Lai C, Bai L, Chen Y (2026) Self-reduced Pd nanoparticles on NiMn-LDHs with superior catalytic activity for signal amplification in electrochemical aptasensing of Mycobacterium tuberculosis ESAT-6 antigen. Microchimica Acta 193:5. https://doi.org/10.1007/s00604-025-07630-y
25. Ye X-A, Lin S-H, Chen L-Y, Li J-R, Chiu H-W, Pan S-W, Feng J-Y, Luo S-C, Ho M-L (2025) Innovative polymer-based electrochemical platform for detecting ESAT-6 in human blood for pulmonary tuberculosis diagnosis. Sensing and Bio-Sensing Research 100816. https://doi.org/10.1016/j.sbsr.2025.100816
26. Broger T, Tsionksy M, Mathew A, Lowary TL, Pinter A, Plisova T, Bartlett D, Barbero S, Denkinger CM, Moreau E (2019) Sensitive electrochemiluminescence (ECL) immunoassays for detecting lipoarabinomannan (LAM) and ESAT-6 in urine and serum from tuberculosis patients. PloS one 14:e0215443. https://doi.org/10.1371/journal.pone.0215443